J. Fluid Mech. (2004), *vol.* 501, *pp.* 355–377.
DOI: 10.1017/S0022112003007535 Printed in the United Kingdom

Evolution of initially axisymmetric buoyancy jets: a numerical study

By M. K. RESZKA AND G. E. SWATERS†

Department of Mathematical & Statistical Sciences, University of Alberta, Edmonton, Alberta T6G 2G1 Canada

(Received 5 December 2002 and in revised form 21 August 2003)

Baroclinic evolution of coastal currents associated with a surface front over variable topography is investigated numerically, employing a two-layer frontal-geostrophic model. In the frontal-geostrophic dynamical limit the frontal layer velocity is geostrophic to leading order; however the advective terms from the momentum equation are accounted for in the leading-order balance, and the mass conservation equation includes both the temporal and advective contributions. In this study, special focus is placed on the role of topography and the development of coherent vortex features. Perturbed axisymmetric currents in an annular domain are seen to develop typical breaking-wave instabilities at the outside edge. In general, the topography is found to be a destabilizing influence; however very steep topography is shown to inhibit cross-front motions, and thus delay subsequent vortex shedding. In simulations involving a continuous source of buoyant fluid, the ambient layer exhibits a marked increase in anticyclonic vorticity, which prevents eddy pinch-off. The results are compared with previous laboratory experiments involving surface currents, and implications for the stability of fronts at a shelf break are discussed.

1. Introduction

Surface-intensified geostrophic currents are a ubiquitous feature of coastal and estuarine dynamics. They are typically associated with a front, i.e. a region of sloped isopycnals exhibiting large horizontal density gradients. This region marks the interface between two water masses that differ in their physical and chemical composition, as well as their origin. A front normally acts as a barrier to diffusion of heat, momentum and chemical and biological tracers; however, when unstable it may promote vigorous large-scale mixing by spawning vortices (Karsten & Swaters 2000). In the case of coastal upwelling, isopycnals slope downward away from the coast. In the present work, we wish to focus on the case of coastally trapped currents, in which buoyant fluid lies adjacent to the coast, with isopycnals rising in the offshore direction, eventually intersecting the surface. In geostrophic equilibrium, the latter configuration induces an along-shore jet flowing with the coast to its right (left) in the northern (southern) hemisphere (Griffiths & Linden 1982).

Most coastally trapped currents owe their existence to an upstream source of relatively fresh water that geostrophically adjusts as it spreads over a deeper ambient layer. This is true of the Norwegian, Algerian, and East Greenland Currents (Johannessen *et al.* 1989; Paldor & Ghil 1991; Wadhams, Gill & Linden 1979). Some

† Also, Institute for Geophysical Research, University of Alberta.

coastally trapped flows are the direct result of river discharge, as is the case with the Gaspé Current and Vancouver Island Coastal Current (Mertz, Gratton & Gagné 1990; Masson & Cummins 1999). Many such surface flows are inherently unstable, and periodically deform due to baroclinic (or sometimes barotropic) energy release, which often leads to significant cross-shore motion and ejection of eddies. Particularly striking examples of vortex shedding can be seen in satellite IR images of the Leeuwin Current off western Australia (Church, Cresswell & Godfrey 1989) and a seasonal slope current along the northern coast of Spain (Pingree & LeCann 1992). Instability of coastally trapped flows can be influenced significantly by the general slope of the underlying continental shelf, the proximity of a shelf break, as well as along-slope topographic variations.

Among the many recent investigations of frontal instabilities at the shelf break is the laboratory study of Cenedese & Linden (2002, henceforth referred to as CL). They conducted experiments on buoyant axisymmetric currents in a rotating two-layer fluid, in order to assess the influence of different topographic configurations on flow evolution. A ring source at the inner wall of the annular domain provided a constant supply of buoyant fluid, which formed a geostrophically balanced azimuthal current. The interface between the buoyant jet and the ambient fluid sloped upward in the radial direction, forming an outcropping front. In addition to flat topography, three configurations were employed for the tank bottom beyond a flat 'shelf' region: a step, a linear slope, and a step adjacent to a slope (see figure 1 in CL). The variable topographies all became deeper in the radial direction so that, in analogy with a continental shelf environment, the inner annulus boundary played the role of a coastline.

After the width of the current reached several Rossby radii, a wave-like instability was always observed at the outcropping (e.g. figure 4 in CL). The instability was believed to be largely baroclinic in nature. The dominant wavelength λ^* was inversely related to the rotational Froude number,

$$F = \frac{f_0^2 L^2}{g' H_1}, \tag{1.1}$$

where f_0, L, g' and H_1 are the Coriolis parameter, current width, reduced gravity and upper-layer thickness scale, respectively. The wavelength was 10–13 times the upper-layer Rossby radius,

$$R_1 = \frac{\sqrt{g' H_1}}{f_0}. \tag{1.2}$$

Dominant lengthscales larger than the deformation radius are indicative of baroclinic instability (Pedlosky 1987). Typically, growth of these waves led to the development of anticyclonic eddies, which sometimes pinched off, while at other times they remained attached to the main body of the jet. Often a train of isolated vortices was reabsorbed, establishing a new axisymmetric front with a larger outside radius. The new wider current was subject to the same kind of instability as the original one.

The experimental results of CL for the flat-bottom case were qualitatively and quantitatively similar to those of Griffiths & Linden (1981, 1982). Griffiths & Linden (1981) explained the observed instabilities in terms of a two-layer quasi-geostrophic (QG) model that included a parameterization for Ekman layers. CL found that step topography (i.e. an idealized shelf break) inhibits the spreading of buoyant fluid, thus trapping it near the coast, at least temporarily. While linearly sloping topography trapped the fluid on the shelf to a lesser degree, it was also found to

impede significantly the instability process. The latter result, while not inconsistent with the usual QG stability criteria (Pedlosky 1964), does seem counterintuitive in the QG context. This point will be discussed further in the present work.

A number of authors have investigated the effects of topography on variability of buoyancy currents. Orlanski (1969) used a two-layer primitive equation model to establish that topography is a stabilizing influence if its cross-shore gradient has the same sign as the fluid interface (i.e. an upwelling front configuration). More pertinent to the present study is the linear analysis of Flagg & Beardsley (1978), who employed a layered shallow-water model with the topography sloping in the opposite sense to the interface (appropriate for a shelf-break front). They found multiple modes of instability, both barotropic and baroclinic. While some of the associated growth rates increased with the bottom slope, the growth rate of the fastest-growing wave was found to decrease.

In contrast, results of Mechoso & Sinton (1981) in a two-layer QG setting indicate that a non-zero topographic gradient tends to be a stabilizing influence compared with the flat-bottom scenario, regardless of its sign. More recently, Gawarkiewicz (1991) re-examined the shelf-break front problem using a primitive equation model, and found a shorter fastest-growing mode than that reported by Flagg & Beardsley (1978). He also determined that the growth rates depend significantly on the shape of the topography, as well as the degree of stratification between the layers. It would appear that a comprehensive theory does not exist which explains the role of topography in all generality (CL).

In the present study we hope to elucidate aspects of the baroclinic dynamics associated with axisymmetric currents in the presence of topography, focusing on the investigation of CL. In particular, we show that the two-layer, frontal formalism used here is able to describe the nonlinear spatio-temporal evolution of initially axisymmetric flows, including eddy pinch-off and fine-scale structures, qualitatively similar to CL and Griffiths & Linden (1981, 1982). We show that, within the assumptions of this formalism, a perturbed steady coastal current tends to be unstable without the necessity of along-front topographic variations. Moreover, instability is enhanced with increasing topography for topographic gradients similar in magnitude (but opposite in sign) to those of the front. For very steep topography, fluid is temporarily trapped on the shoreward side due to the associated high potential vorticity (PV) gradient. We derive necessary conditions for instability in the linearized, axisymmetric regime and relate these to the traditional QG criteria. Our simulations suggest that the inclusion of a source of buoyant fluid inhibits eddy detachment, in agreement with CL. We also analyse the effect of various topographic configurations on cross-slope and along-shore transports.

The paper is organized as follows. We describe our theory and discuss the associated linearized equations in § 2. Simulations of axisymmetric currents using the full nonlinear governing equations are presented in § 3. Section 4 consists of a general discussion of the role of topography from the point of view of quasi-geostrophic dynamics. Conclusions are given in § 5.

2. Model description

2.1. *Governing equations*

The governing equations used here correspond to an asymptotic reduction of the two-layer shallow-water system in the small Rossby number regime. This theory models the release of available potential energy stored in a sloping fluid interface, and subsequent

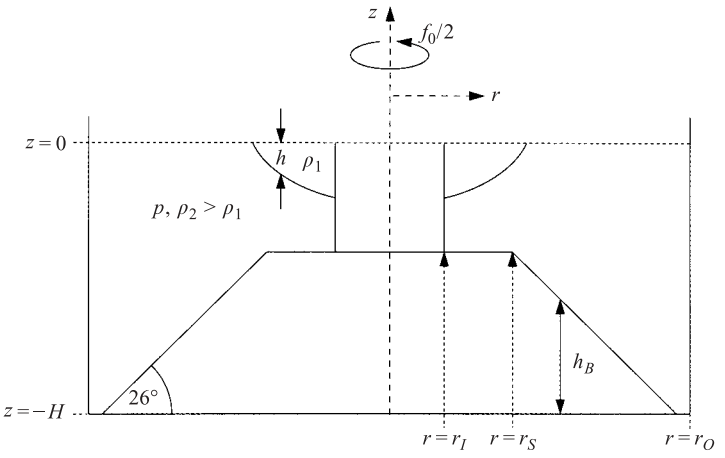

FIGURE 1. Vertical cross-section of the computational domain showing a typical profile of the initial current and shelf-slope bottom topography. Flat topography and step topography, which deepens at $r = r_S$, were also considered. Numerical values for all the parameters are given in the text.

two-way interaction between the fluid layers, allowing for large-amplitude dynamic deflections of the interface. The model geometry is shown in figure 1. Velocities are assumed to be geostrophic to leading order, and the lower layer is governed by QG dynamics. However the upper layer is not QG, in that the dynamic deflections of the interface scale as the upper-layer thickness itself.

The model derivation, stability criteria, and the associated Hamiltonian structure were presented in Swaters (1993) (a variant of the model appropriate for beta-plane dynamics was independently derived by Cushman-Roisin, Sutyrin & Tang 1992). Reszka (2003) has described a generalization of the governing equations which allows for stratification in the ambient fluid as well as mass sources and sinks. A general and rigorous derivation of two-layer frontal models from the primitive equations on a sphere can be found in Karsten & Swaters (1999). Here we provide only highlights of the derivation, and the reader is referred to the above papers for more complete details.

The shallow-water equations are non-dimensionalized so that lower-layer velocity is driven by vortex stretching associated with a deforming interface in the presence of a topographic vorticity gradient. Griffiths & Linden (1982) found that the size of eddies in their experiments scaled naturally with the geometric mean of the upper- and lower-layer Rossby radii. The trend was most pronounced for large values of the Froude number, which is the regime described here. This motivates our choice of lengthscale,

$$L_* = \sqrt{R_1 R_2}, \tag{2.1}$$

where R_1 was defined above and

$$R_2 = \frac{\sqrt{g' H_2}}{f_0} \tag{2.2}$$

is the lower-layer deformation radius, with H_2 being the scale depth of the lower layer. Given (2.1), the upper-layer velocity scaling ensures that leading-order velocities are geostrophic but that ageostrophic velocity corrections associated with the advective

terms are also incorporated in the final balance. This dynamical regime is known as the frontal geostrophic (henceforth FG) approximation (Cushman-Roisin 1986).

In terms of the depth fraction,

$$\delta = H_1/H, \tag{2.3}$$

where $H = H_1 + H_2$, the non-dimensional equations may be written as

$$\delta \boldsymbol{u}_{1t} + \delta^{1/2}\boldsymbol{u}_1 \cdot \nabla \boldsymbol{u}_1 + \boldsymbol{e}_3 \times \boldsymbol{u}_1 = -\nabla\varphi, \tag{2.4a}$$

$$\delta^{1/2} h_t + \nabla \cdot (\boldsymbol{u}_1 h) = \delta^{1/2} Q, \tag{2.4b}$$

$$\delta \boldsymbol{u}_{2t} + \delta \boldsymbol{u}_2 \cdot \nabla \boldsymbol{u}_2 + \boldsymbol{e}_3 \times \boldsymbol{u}_2 = -\nabla p, \tag{2.4c}$$

$$\nabla \cdot \boldsymbol{u}_2 = \delta h_t + \delta \nabla \cdot [\boldsymbol{u}_2 (h_B + h)], \tag{2.4d}$$

$$\varphi = h + \delta^{1/2} p, \tag{2.4e}$$

where $\boldsymbol{u}_1$ and φ are the upper-layer velocity and dynamic pressure, $\boldsymbol{u}_2$ and p are the lower-layer velocity and dynamic pressure, while h is the thickness of the upper layer and h_B is the height of bottom topography above a fixed reference level. Here $Q(x, y)$ represents a source of upper-layer (buoyant) fluid. The dimensionalized integral of the source distribution Q over the domain will be referred to as $\overline{Q}^*$, or the source strength. A sink of lower-layer (ambient) fluid may be introduced in (2.4*d*), with a distribution that ensures overall mass conservation (see Reszka 2003). However, to be consistent with the experimental procedure of CL, we do not consider sinks in this study, i.e. the overall volume of the fluid will grow if the prescribed distribution $Q(x, y)$ is such that $\overline{Q}^* > 0$.

Assuming a small δ, the first non-trivial PV balance in the leading-order fields constitutes the governing prognostic equations

$$[\partial_t + J(p, *)]\, h + \nabla \cdot [h J(\nabla h, h)] = Q, \tag{2.5a}$$

$$[\partial_t + J(p, *)]\, (\nabla^2 p + h + h_B) = 0, \tag{2.5b}$$

where $J(A, B) = A_x B_y - A_y B_x$ is the usual Jacobian operator. Here, h and p are streamfunctions, such that

$$\boldsymbol{u}_1 = \boldsymbol{e}_3 \times \nabla h \quad \text{and} \quad \boldsymbol{u}_2 = \boldsymbol{e}_3 \times \nabla p. \tag{2.6}$$

To leading order, the lower-layer PV in this model is $\nabla^2 p + h + h_B$, while the upper-layer PV is $1/h$. Thus (2.5*a*) may be thought of as the evolution equation for the upper-layer PV, as well as the mass conservation equation for the frontal layer. These are the equations that will be solved numerically in § 3, where we will also discuss appropriate boundary conditions. However we point out that the boundary condition for the upper layer at any outcropping simply reduces to (2.5*a*) itself (Swaters 1993). Thus no additional computation is necessary in order to track the time evolution of the outcropping. We note that, because we have assumed $\delta \ll 1$, i.e. $H_2 \approx H$, the leading-order balance (2.5*a*)–(2.5*b*) may also be derived using the definition $\delta = H_1/H_2$.

2.2. *Linear stability*

We examine the linear stability problem for initially axisymmetric flows. Equations (2.5*a*), (2.5*b*) are written in terms of polar coordinates (r, θ), where $r = \sqrt{x^2 + y^2}$ and $\tan(\theta) = y/x$. The domain will be the annulus $\Omega = \{(r, \theta) | r_I \leqslant r \leqslant r_O\}$, where r_I^*, r_O^* and Ω^* are the dimensional analogues of r_I, r_O and Ω, respectively. Previous

numerical studies involving (2.5*a*), (2.5*b*) have shown that along-front topographic variations are not necessary for the growth of instabilities (Reszka & Swaters 1999).

Assuming topography of the form $h_B = h_B(r)$, the governing equations may be written as

$$h_t = J\left(h,\, p + h\nabla^2 h + \tfrac{1}{2}\nabla h \cdot \nabla h\right) + Q, \tag{2.7a}$$

$$(\nabla^2 p + h)_t = J(\nabla^2 p + h,\, p) + \frac{1}{r}\frac{\mathrm{d}h_B}{\mathrm{d}r} p_\theta + 0, \tag{2.7b}$$

where $\nabla = (\partial_r,\, \partial_\theta / r)$, $\nabla^2 = \partial_r(r\partial_r)/r + \partial_\theta^2 / r^2$, and $J(A,\, B) = (A_r B_\theta - A_\theta B_r)/r$. Radial velocities in the upper and lower layers are now defined in terms of the streamfunctions as

$$u_{1r} = -\frac{1}{r}\frac{\partial h}{\partial \theta} \quad \text{and} \quad u_{2r} = -\frac{1}{r}\frac{\partial p}{\partial \theta}, \tag{2.8}$$

respectively. Upper- and lower-layer azimuthal velocities (positive in the counter-clockwise direction) are given by

$$u_{1\theta} = \frac{\partial h}{\partial r} \quad \text{and} \quad u_{2\theta} = \frac{\partial p}{\partial r}. \tag{2.9}$$

In the absence of sources and sinks, $\{h = h_0(r),\ p = p_0(r)\}$ comprises an exact steady solution to (2.5*a*)–(2.5*b*), for sufficiently smooth functions h_0, p_0. We consider a perturbed steady state, by making the substitution

$$(h,\, p) = (h_0(r),\, 0) + (h',\, p')(r, \theta, t), \tag{2.10}$$

where $h',\, p' \ll 1$. In order to focus on the baroclinic aspect of the problem, there is no imposed mean flow in the lower layer.

The interface does not have to outcrop; however if it does, we will assume the outcropping is located at $r = b \in (r_I, r_O)$. If $h > 0$ for $r \in [r_I, b)$, then we shall consider h to be defined but zero for $r \in [b, r_O]$. Thus, h is defined and continuous on the entire domain, although its radial derivative may be discontinuous at the outcropping. Then, dropping the primes, the linearized stability equations become

$$r h_t - \frac{\mathrm{d}h_0}{\mathrm{d}r} p_\theta + \left[\frac{\mathrm{d}}{\mathrm{d}r}\left(h_0 \frac{\mathrm{d}^2 h_0}{\mathrm{d}r^2}\right) + h_0 \frac{\mathrm{d}}{\mathrm{d}r}\left(\frac{1}{r}\frac{\mathrm{d}h_0}{\mathrm{d}r}\right) - h_0 \frac{\mathrm{d}h_0}{\mathrm{d}r}\nabla^2 - \left(\frac{\mathrm{d}h_0}{\mathrm{d}r}\right)^2 \partial_r\right] h_\theta = 0, \tag{2.11a}$$

$$r(\nabla^2 p + h)_t - \frac{\mathrm{d}}{\mathrm{d}r}(h_B + h_0) p_\theta = 0. \tag{2.11b}$$

The upper-layer perturbation energy equation is formed as follows. Equation (2.11*a*) is multiplied by h/r and integrated over the domain. Employing integration by parts, the result may be written

$$\int\!\!\int_\Omega r h h_t \,\mathrm{d}r\,\mathrm{d}\theta = \int\!\!\int_\Omega \frac{\mathrm{d}h_0}{\mathrm{d}r} p_\theta h \,\mathrm{d}r\,\mathrm{d}\theta + \int\!\!\int_\Omega h_0 \left(\frac{\mathrm{d}^2 h_0}{\mathrm{d}r^2} - \frac{1}{r}\frac{\mathrm{d}h_0}{\mathrm{d}r}\right) h_r h_\theta \,\mathrm{d}r\,\mathrm{d}\theta, \tag{2.12}$$

where we have used the azimuthal periodicity of all fields and the fact that the perturbation vanishes on the radial boundaries.

Defining the integral operator

$$\langle (*) \rangle = \int_0^{2\pi} (*) r \,\mathrm{d}\theta, \tag{2.13}$$

and using (2.8) and (2.9), we obtain

$$\frac{\mathrm{d}}{\mathrm{d}t}\int_{r_I}^{r_O}\tfrac{1}{2}\langle h^2\rangle\,\mathrm{d}r = -\int_{r_I}^{r_O} r\frac{\mathrm{d}}{\mathrm{d}r}\left(\frac{1}{r}\frac{\mathrm{d}h_0}{\mathrm{d}r}\right)\langle h_0 u_{1r}u_{1\theta}\rangle\,\mathrm{d}r - \int_{r_I}^{r_O}\frac{\mathrm{d}h_0}{\mathrm{d}r}\langle u_{2r}h\rangle\,\mathrm{d}r, \tag{2.14}$$

where $\langle h_0 u_{1\theta}u_{1r}\rangle$ represents the along-coast perturbation Reynolds stress. Our interpretation of this equation is similar to Swaters (1993) for the analogous result in rectangular coordinates. Assume that baroclinic processes dominate (the first term on the right-hand side is small) and that the current thickness decreases offshore, i.e. $\mathrm{d}h_0/\mathrm{d}r < 0$. Growth of perturbations (positive left-hand side) requires that, on average, $\langle u_{2r}h\rangle$ and $\mathrm{d}h_0/\mathrm{d}r$ are negatively correlated. Therefore, there must be a net offshore flux of warm anomalies ($h > 0$) by the geostrophic velocity u_{2r}.

A necessary condition for instability may be derived by first making the normal-mode assumption with respect to azimuthal flow,

$$(h,\,p) = (\tilde{h},\,\tilde{p})(r)\exp[\mathrm{i}n(\theta - ct)] + \text{c.c.}, \tag{2.15}$$

where n is the integer azimuthal wavenumber, c is the (complex) phase speed and c.c. refers to the complex conjugate. Then, dropping the tildes, we have

$$crh + \frac{\mathrm{d}h_0}{\mathrm{d}r}p - \frac{\mathrm{d}}{\mathrm{d}r}\left(h_0\frac{\mathrm{d}^2h_0}{\mathrm{d}r^2}\right)h - h_0\frac{\mathrm{d}}{\mathrm{d}r}\left(\frac{1}{r}\frac{\mathrm{d}h_0}{\mathrm{d}r}\right)h + h_0\frac{\mathrm{d}h_0}{\mathrm{d}r}\left[h_{rr} + \frac{1}{r}h_r - \frac{n^2}{r^2}h\right] + \left(\frac{\mathrm{d}h_0}{\mathrm{d}r}\right)^2 h_r = 0, \tag{2.16a}$$

$$c\left(rp_{rr} + p_r + \frac{1}{r}p_{\theta\theta} + rh\right) + \frac{\mathrm{d}}{\mathrm{d}r}(h_B + h_0)p = 0. \tag{2.16b}$$

Similarly to Swaters (1993), we define a function $\widehat{h}(r)$ by

$$h(r) = \frac{\mathrm{d}h_0}{\mathrm{d}r}\widehat{h}(r), \tag{2.17}$$

substitution of which will simplify the algebraic expressions below. We multiply the complex conjugate of (2.16*a*) by $r\widehat{h}$ and integrate over $r_I < r < r_O$. After integration by parts, using the fact that the perturbation (and therefore $\widehat{h}$) vanishes on the boundaries, the result is

$$\int_{r_I}^{r_O} h_0\left(\frac{\mathrm{d}h_0}{\mathrm{d}r}\right)^2\left(\frac{n^2}{r}|\widehat{h}|^2 + r|\widehat{h}_r|^2\right)\mathrm{d}r - \int_{r_I}^{r_O}\left(c^*r^2\frac{\mathrm{d}h_0}{\mathrm{d}r} + \frac{1}{r}h_0\left(\frac{\mathrm{d}h_0}{\mathrm{d}r}\right)^2\right)|\widehat{h}|^2\,\mathrm{d}r = \int_{r_I}^{r_O} r\frac{\mathrm{d}h_0}{\mathrm{d}r}p^*\widehat{h}\,\mathrm{d}r. \tag{2.18}$$

Similarly, multiplying (2.16*b*) by p^*/c (assuming $|c|^2 > 0$), integrating with respect to r, and using integration by parts, we obtain

$$\int_{r_I}^{r_O}\left(r|p_r|^2 + \frac{1}{r}|p_\theta|^2\right)\mathrm{d}r - \frac{1}{c}\int_{r_I}^{r_O}\frac{\mathrm{d}}{\mathrm{d}r}(h_B + h_0)|p|^2\,\mathrm{d}r = \int_{r_I}^{r_O} r\frac{\mathrm{d}h_0}{\mathrm{d}r}p^*\widehat{h}\,\mathrm{d}r. \tag{2.19}$$

If we subtract (2.19) from (2.18), substitute in $c = c_R + \mathrm{i}c_I$, and take the imaginary part of the resulting equation, then

$$c_I\int_{r_I}^{r_O}\left(r^2\frac{\mathrm{d}h_0}{\mathrm{d}r}|\widehat{h}|^2 - \frac{1}{|c|^2}\frac{\mathrm{d}}{\mathrm{d}r}(h_B + h_0)|p|^2\right)\mathrm{d}r = 0. \tag{2.20}$$

Let us assume that we are dealing with a coastally trapped current, such that the frontal thickness decays away from the shore, $\mathrm{d}h_0/\mathrm{d}r < 0$. Then

$$\frac{\mathrm{d}h_B}{\mathrm{d}r} > -\frac{\mathrm{d}h_0}{\mathrm{d}r} \quad \text{for all } r \in (r_I, r_O) \tag{2.21}$$

is a sufficient condition for stability. Conversely, a necessary condition for instability is that

$$\frac{\mathrm{d}h_B}{\mathrm{d}r} \leqslant -\frac{\mathrm{d}h_0}{\mathrm{d}r}, \tag{2.22}$$

for at least one $r \in (r_I, r_O)$. This result is analogous to the one derived in Swaters (1993), and as we discuss in § 4, it is consistent with the QG necessary condition for instability (Pedlosky 1964) that the PV gradients be of opposite sign in the two layers.

3. Simulations of axisymmetric currents

In this section we address the following issues associated with frontal instability, as found in our simulations. Following a discussion of the numerics, the basic features of the instability are described and compared with those observed by CL and Griffiths & Linden (1981). The effects of topography on both the initial and nonlinear stages of instability are investigated. Gross features of the flow, as well as derived diagnostics, suggest that the basic baroclinic mechanism captured in our model reproduces several of the processes observed by CL, such as formation of anticyclonic eddy features a few Rossby radii in width, gradual outward motion of the eddies, and a temporary halting of wave growth in the presence of ridge topography. One diagnostic computed is the along-front transport as a function of time. While this is not a quantity discussed by CL, the evolution of eddy-induced transports is of general interest, and has recently received much attention in the context of the Antarctic Circumpolar Current (e.g. Hallberg & Gnanadesikan 2001).

Trends with respect to topography are similar for simulations with and without a source of buoyant fluid. However, those that do involve a source indicate more pronounced anticyclonic motions at finite amplitude and a smaller propensity for eddy detachment, which is consistent with the findings of CL. The latter effect is also reasonable on theoretical grounds since, without a source, developing dipoles in the ambient fluid can self-propel radially outward, whereas with a source, increasing current thickness causes a dominance of anticyclonic anomalies and therefore less self-advection. An important difference between our observations and those of CL is that our model predicts (analytically and numerically) an increase in growth rates with the topographic slope. CL, on the other hand, found that sloping topography suppressed the instability. We discuss possible reasons for this discrepancy.

3.1. *Numerical procedure*

We employed the nonlinear model equations (2.5*a*)–(2.5*b*) in a series of numerical simulations in order to explore the instability of a buoyant axisymmetric current, in a configuration similar to the laboratory experiments of CL. The governing equations were solved in Cartesian rectangular coordinates, using a finite difference scheme with explicit time-stepping and Arakawa (1966) Jacobians. No-slip boundary conditions were applied at the walls and the lower-layer streamfunction was recovered from the potential vorticity via a Conjugate Gradient elliptic solver (Kincaid & Cheney 1996). Numerical friction proportional to $\nabla^2 h$ and $\nabla^8 h$ was employed in (2.5*a*) with coefficients 2×10^{-7} and 5×10^{-11}, respectively.

The computational domain was an annulus, centred at the origin, whose dimensional inner and outer radii were, respectively, $r_I^* = 13\,\text{cm}$ and $r_O^* = 45\,\text{cm}$, as in CL. Two sets of simulations were performed, one that did not include an upper-layer source (SERIES 1), and one where the source strength was $\overline{Q}^* = 10\,\text{cm}^3\,\text{s}^{-1}$ (SERIES 2). As mentioned previously, a sink was not prescribed in the lower layer in either series. Thus, total mass is not conserved in SERIES 2, in keeping with the experiments of CL. In all our simulations we assume the scalings $H_1 = 3.5\,\text{cm}$ and $H = 13.0\,\text{cm}$ with $g' = 2.2\,\text{cm}\,\text{s}^{-2}$ and $f_0 = 3.0\,\text{rad}\,\text{s}^{-1}$, which are mid-range parameter values in the experiments of CL. Here, H_1 is taken to be the maximum depth of the upper layer at $t = 0$ (i.e. its depth at the inner wall). The depth fraction, upper-layer Rossby radius and dynamic lengthscale are then $\delta = 0.27$, $R_1 = 0.93\,\text{cm}$ and $L_* = 1.28\,\text{cm}$, respectively. The spatial resolution was 240×240, for a grid spacing of 0.375 cm.

Some of our modelling assumptions are not met in the CL experiments, and consequently, direct comparisons should be made with caution. In particular, since we assume that the velocity is geostrophic, the outward pressure gradient associated with an imposed source (SERIES 2) does not induce spreading of the surface layer. Due to the assumed dominance of rotational effects in the model, the velocity has no component along the pressure gradient (although ageostrophic effects are key in the evolution of the PV field (see Swaters 1993). As we can only simulate lateral growth after instability has occurred, we prescribe a current profile as an initial condition in both SERIES 1 and SERIES 2, such that the current width is consistent with CL's experimental values at the onset of instability. A similar approach was taken by Verzicco, Lalli & Campana (1997). A constant source of upper-layer fluid does, however, allow us to explore the transition to instability while the fluid depth (and therefore the effective Rossby radius) is increasing. Thus in SERIES 2 a source of buoyant fluid is introduced, with the same strength as in CL.

Another point to remember is that, in the experiments of CL, the upper layer often touches the shallow part of the topography before instability occurs, which undoubtedly affects the ensuing dynamics. Contact with a bottom boundary induces drag and Ekman draining, both processes being absent in the present model. Our derivation also assumes that the lower layer is everywhere thicker than the upper layer, which is clearly not the case when the upper layer and topography meet. Our results are therefore most relevant to the laboratory trials in which the buoyant fluid did not touch the bottom. However, it should be stressed that the results of CL do not show a marked difference between these two dynamical regimes. Finally, in SERIES 1 the initial current depth at the coast was maintained in time. The condition of no-normal-flow required the azimuthal derivative of the upper-layer thickness to be zero along the boundary. Since there is no unique way to determine the temporal depth change of the current as a whole at the coast, we chose the simplest condition, i.e. no depth change with time.

The initial, non-dimensional frontal profile is given by

$$h_0(r) = \alpha \max\{1 - \exp[\gamma(r - b)], 0\}, \tag{3.1}$$

where $r = b$ is the location of the outcropping, α controls the overall thickness of the front while γ is a measure of its steepness. We choose the parameters so that the jet has a dimensional width of about 10 cm and its depth at the coast is exactly 3.5 cm, i.e. $\alpha = 1.021$ and $b = 17.891$. In simulations with flat topography, the lower-layer depth varies between 9.5 cm at the coast and 13.0 cm at the offshore boundary. For simulations with shelf topography, the thickness of the lower layer is 0 cm at the

Simulation	$\overline{Q}^*$ ($\mathrm{cm^3\,s^{-1}}$)	r_S (cm)	λ^* (cm)
flat1	0	N/A	7.2
step1-I	0	20.0	4.5
step1-O	0	22.9	3.6
slope1-I	0	20.0	6.0
slope1-O	0	22.9	6.5
flat2	10.0	N/A	7.2
step2-I	10.0	20.0	5.1
step2-O	10.0	22.9	3.6
slope2-I	10.0	20.0	6.5
slope2-O	10.0	22.9	7.2

TABLE 1. Configuration of numerical simulations and observed dominant wavelength, pertaining to axisymmetric currents in an annulus domain. For simulations designated 'step' or 'slope', r_S is the radius at which the topography deepens abruptly or becomes linearly sloping, respectively. The step has a depth of 9.5 cm while the sloping topography has a radial gradient of -0.5. Here $\overline{Q}^*$ is the source strength and λ^* is the dominant along-front wavelength.

coast, 3.5 cm at the shelf break and 13.0 cm at the offshore boundary. We fix $\gamma = 0.5$ which gives a maximum initial current velocity of approximately 1 $\mathrm{cm\,s^{-1}}$.

Our simulations are designated with the names 'flat', 'step' and 'slope', which refer to the three kinds of topography we consider. The names and their corresponding configurations are given in table 1. The number within each name refers to the absence (1) or presence (2) of the source term. Finally, there are two possible locations, $r = r_S$, of the step or top of the slope. These are on the inner side (designated 'I') of the front, about two Rossby radii away from the outcropping, or on the outer side (designated 'O') of the front, exactly at the outcropping. The step will also be referred to as a ridge, or shelf break, while the region interior to the step (or slope) will be identified as a continental shelf.

3.2. *Description of the instability*

Here we give a detailed description of simulation step1-I, which was typical, and which will serve as the standard case for later comparisons. In figure 2 we plot the dimensional upper-layer thickness, at (dimensional) times $t/P = 0$, 12, 18 and 24 (where P is the rotation period), while the corresponding contour plots of non-dimensional lower-layer pressure are displayed in figure 3. We note that one rotation period P corresponds to 4.2 s in all the simulations described here. Initially, a steady axisymmetric current profile is imposed on the upper-layer streamfunction (figure 2*a*). There is no mean flow in the lower layer; however we seed its pressure field with a small-amplitude random perturbation (figure 3*a*). The initial perturbation amplitude is scaled so that its area-integrated kinetic energy is 4 orders of magnitude smaller than the area-integrated kinetic energy of the current, i.e.

$$\int\!\!\int_{\Omega} \nabla p \cdot \nabla p r \,\mathrm{d}r\,\mathrm{d}\theta = 10^{-4} \int\!\!\int_{\Omega} h \nabla h \cdot \nabla h r \,\mathrm{d}r\,\mathrm{d}\theta. \tag{3.2}$$

This allows the most unstable mode to develop before nonlinear effects become important.

After 12 rotation periods, the dominant mode has emerged and the outcropping is deformed by a wave-like disturbance. Wave crests are seen to break backwards in relation to the mean flow of the jet, behaviour consistent with the findings of CL

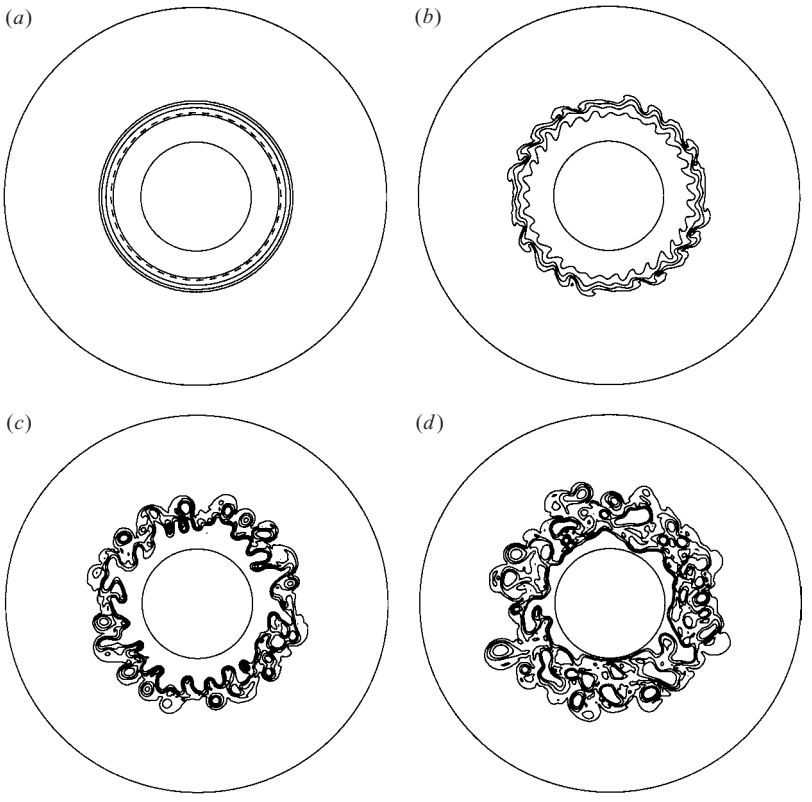

FIGURE 2. Dimensional upper-layer thickness in simulation step1-I at (*a*) 0, (*b*) 12, (*c*) 18 and (*d*) 24 rotation periods. The contour range is 0 to 3.5 cm and the contour interval is 0.875 cm. The dashed contour in (*a*) marks the location of the step.

and Griffiths & Linden (1981) (figure 2*b*). The lower layer exhibits a regular pattern of high- and low-pressure anomalies along the shoreward side of the outcropping (figure 3*b*). Each pair of pressure cells is a dipole, whose natural tendency is to self-advect in a cross-front direction. Growth of the upper-layer meanders continues and some of the waves merge with their neighbours.

Gradual strengthening of lower-layer dipoles and their subsequent deformation aids in a build-up of anticyclonic vorticity at the wave crests. Some of the breaking waves eventually pinch off as coherent vortices. The first eddies appear at about $t/P = 15$, although these are quickly reabsorbed by the current. Sustained instability leads to numerous new upper-layer eddies, seen in figure 2(*c*), which begin to move away from the jet. By this time the lower layer is showing signs of the red energy cascade, with many adjacent pressure anomalies merging together (figure 3*c*). Growth of the dominant lengthscale over the course of the instability was observed in the laboratory setting by, for example, Griffiths & Linden (1982). They found the effect to be more pronounced in the large Froude number regime. Returning to figure 3, upper-layer lenses continue to pinch off, and are often observed to merge together or split apart. Elongated eddies that merge with protrusions of the main body of the current appear as filaments (figure 2*d*).

After 24 rotation periods the buoyant flow may best be described as a turbulent eddy field, whose individual features are advected around by large, prominent gyres

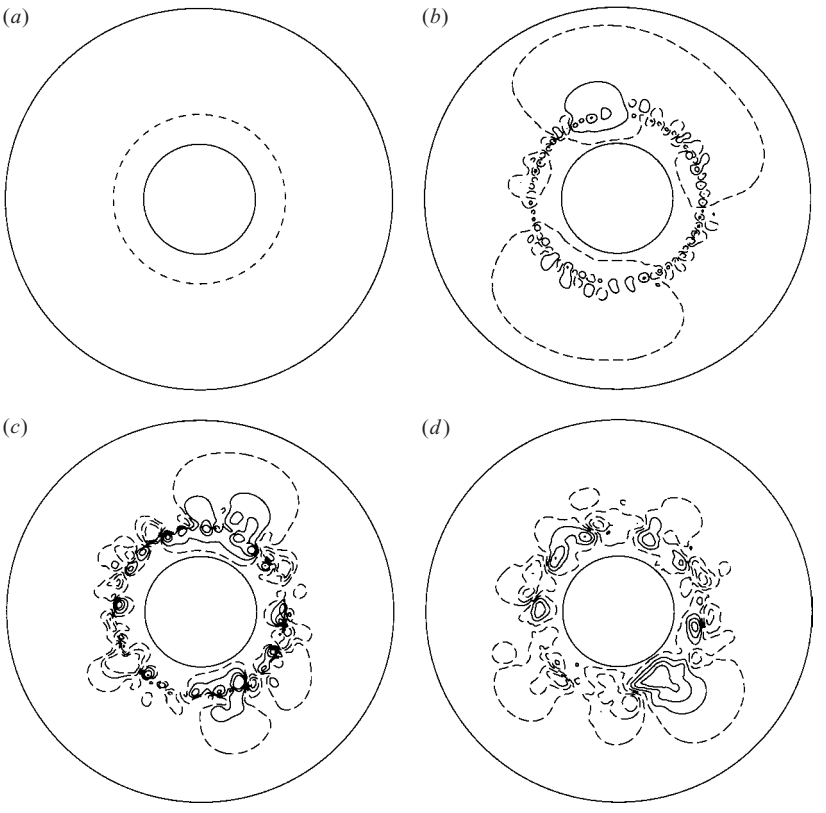

FIGURE 3. (*a*) Location of the topographic step. (*b–d*) Non-dimensional lower-layer pressure in simulation step1-I at (*b*) 12, (*c*) 18 and (*d*) 24 rotation periods. The contour extrema and intervals are, respectively, (*b*) −0.43, 0.44, 0.145, (*c*) −0.96, 0.96, 0.32, (*d*) −2.0, 2.8, 0.8. Dashed lines correspond to negative values in (*b–d*). At $t = 0$ the lower-layer pressure consists of a random superposition of radial and azimuthal modes with very small amplitude.

which now dominate the ambient fluid (figure 3*d*). Eddy generation slows down as the jet becomes very narrow; however instabilities of the frontal region still occur toward the end of the simulation, at 30 rotation periods. We remind the reader that the eddies which appear in figures 2(*c*) and 2(*d*) are isolated upper-layer features, not simply interfacial anomalies as in QG-layer models. A high resolution was specified for these simulations specifically to capture the fine-scale structure of these flows. At late times the flow is reminiscent of geostrophic turbulence. A discussion of geostrophic turbulence in the two-layer FG limit may be found in Tang & Cushman-Roisin (1992). In particular, these authors show that a field of FG eddies may retain its turbulent character indefinitely, in contrast to similar QG systems. Plots of the streamfunctions at $t/P = 30$ are given in figure 4, and show little change in upper-layer flow, except a general outward spreading.

In the above simulation the ridge was located shoreward of the front. The behaviour of the evolving current is markedly different when the ridge lies at the same radius as the outcropping. The upper- and lower-layer streamfunctions for simulation step1-O at $t/P = 20$ are plotted in figure 5. The instability appears confined to the shelf region, and upper-layer meanders do not protrude as far in the radial direction as they do in step1-I at the same stage of instability. The same phenomenon was

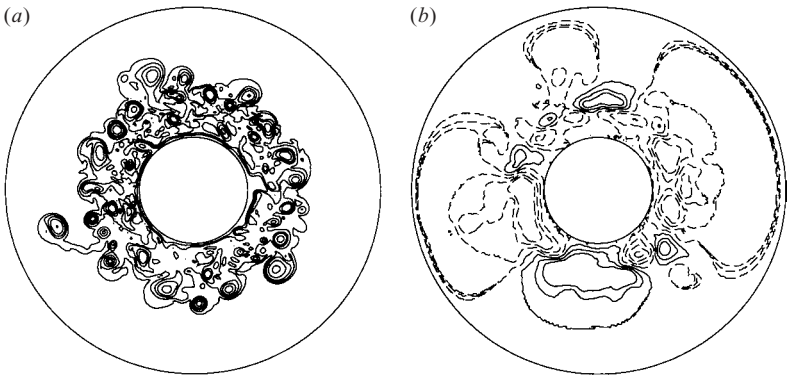

FIGURE 4. (*a*) Dimensional upper-layer thickness and (*b*) non-dimensional lower-layer pressure in simulation step1-I at 30 rotation periods. The contour extrema and intervals are (*a*) 0, 3.5, 0.875 cm and (*b*) −2.8, 2.8, 0.8, respectively.

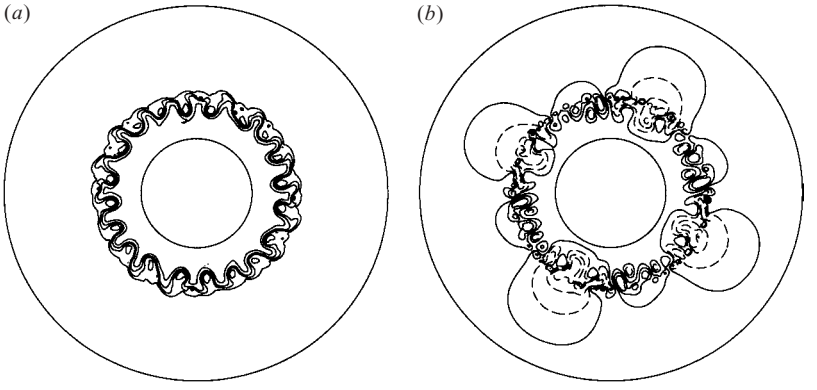

FIGURE 5. (*a*) Dimensional upper layer thickness and (*b*) non-dimensional lower layer pressure in simulation step1-O at 20 rotation periods. The contour extrema and intervals are, respectively, (*a*) 0, 3.5 and 0.875 cm, and (*b*) −0.45, 0.45 and 0.15. Dashed lines correspond to negative values. The initial profile for the upper-layer thickness is the same as in figure 2(*a*) and the topographic step coincides with the initial outcropping.

observed by CL, and was attributed to the greater energy requirement associated with motion across the ridge. Crossing the shelf break induces a significant spin up (spin down) of the ambient fluid due to the stretching (compression) of vortex tubes. We believe this is the mechanism that traps fluid on the shelf in our simulations, until the jet has released enough potential energy to allow robust radial motions across the high topographic PV gradient. We note that, on a finite discretization grid, the topographic step is not a true discontinuity, and appears as a very steep slope of width Δx. Eventually, meanders pinch off forming eddies, and the spreading of the buoyant fluid progresses similarly to step1-I.

All of our SERIES 1 simulations show prominent eddy detachment following the initial growth of meanders, with the exception of simulation step1-O where a noticeable delay occurs, as described above. In figure 6 we have plotted the current thickness and ambient pressure fields for simulation flat1 (i.e. flat topography) at $t/P = 15$ and 24. This simulation is analogous to the experiments of Griffiths &

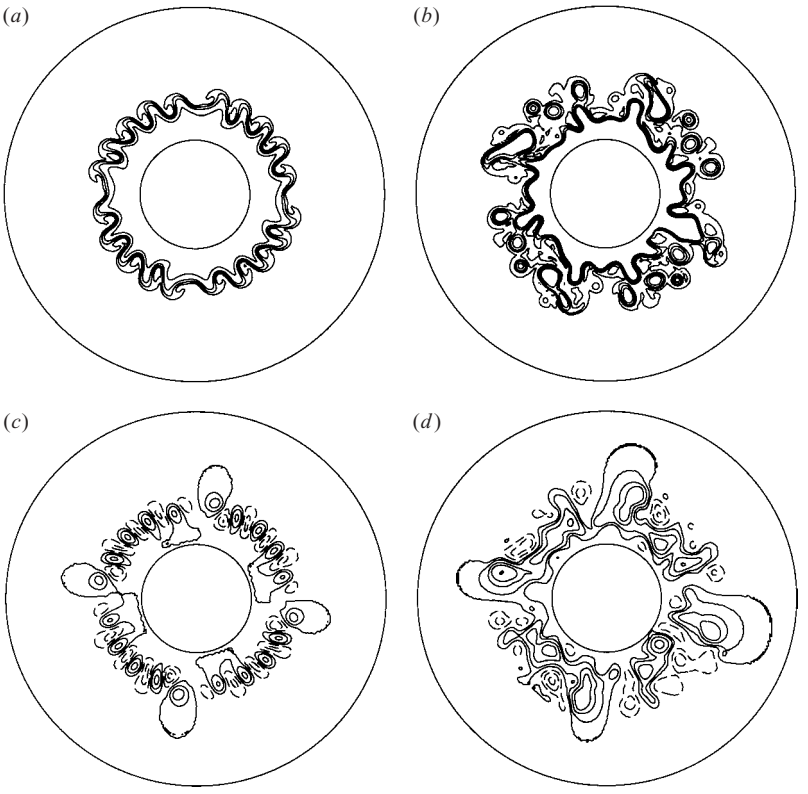

FIGURE 6. (*a*, *b*) Dimensional upper-layer thickness at (*a*) 15 and (*b*) 24 rotation periods: (*c*, *d*) non-dimensional lower layer pressure at (*c*) 15 and (*d*) 24 rotation periods in simulation flat1. The contour extrema and intervals are, respectively, (*a*) 0, 3.5 and 0.875 cm, (*b*) 0, 3.5 and 0.875 cm, (*c*) 0, 0.42 and 0.14, (*d*) 0, 0.99 and 0.33. The initial profile for the upper layer is exactly as shown in figure 2(*a*).

Linden (1981) and demonstrates that the same kind of instability as described above occurs without topographic features as well. Additionally, we can compare these plots with those from simulation flat2 (figure 8), where a source of buoyant fluid is present. In figure 6, backward-breaking waves are visible in (*a*) and multiple fully detached eddies are apparent in (*b*). As table 1 indicates, the presence of topography shoreward of the front decreases the lengthscale of the initial instability; however the resulting eddies in simulations flat1 and step1-I are similar in size.

In experiments with flat topography, CL found that eddies generated by the instability did not detach and move away from the current, while Griffiths & Linden (1981) observed fully detached eddies only for very long waves. A possible explanation for this discrepancy with our simulations is the presence of a source flux in CL's experiments. As it moved radially outward, the outside edge of the main body of the current may have impinged on the developing eddies, and thus hindered detachment. Turbulence, though weak, caused by the constant injection of fluid, may also have contributed to a saturation of the instability, which suppressed eddy pinch-off. Finally, the spreading and deepening of the fluid caused by the source probably resulted in a continual increase of the effective Rossby radius, thus affecting the dominant lengthscales of the instability. We explore this issue further in § 3.4 where we find

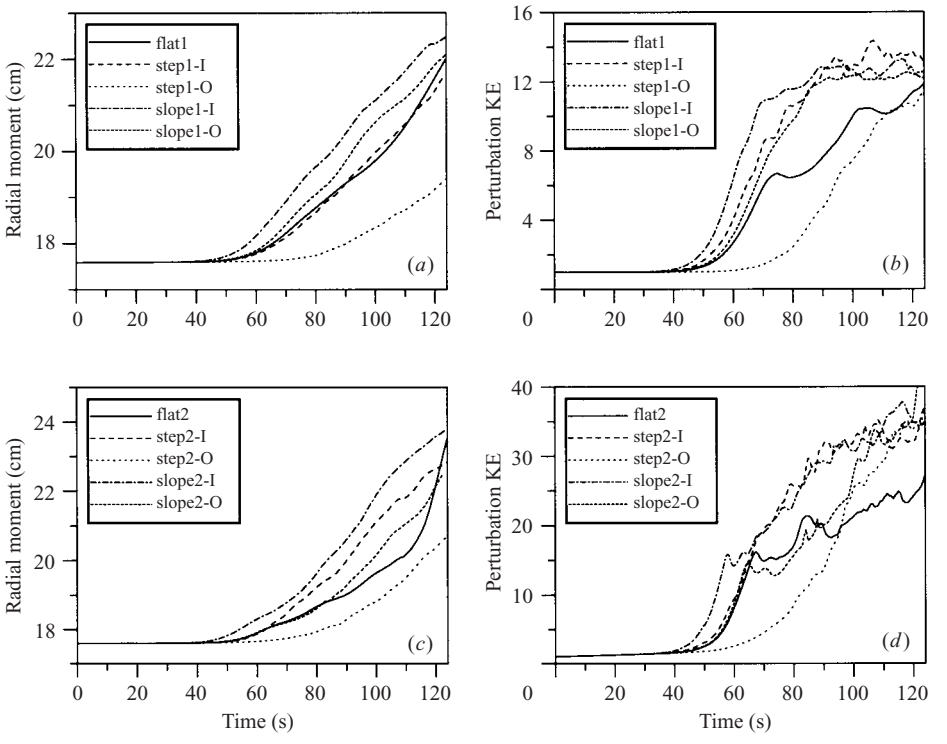

FIGURE 7. (*a*) Dimensional upper-layer radial moment, (*b*) non-dimensional upper-layer kinetic energy for simulation SERIES 1; (*c*) dimensional upper-layer radial moment, (*d*) non-dimensional upper-layer kinetic energy for simulation SERIES 2.

that growing eddy features remain attached and are subsequently reabsorbed by the mean flow, when a source of buoyant fluid is introduced.

3.3. *Influence of topography*

In order to quantify the amount of offshore spreading due to the instability for various topographic configurations, we have computed the average radial moment of the buoyant fluid, defined by

$$\overline{R}(t) = \frac{1}{V}\int\int_{\Omega} r^2 h \, \mathrm{d}r \, \mathrm{d}\theta, \tag{3.3}$$

where $h(r, \theta, t)$ is the total upper-layer thickness and V is the (constant) volume of the upper layer,

$$V = \int\int_{\Omega} r h \, \mathrm{d}r \, \mathrm{d}\theta. \tag{3.4}$$

The integral in (3.3) is essentially the average radius over the volume of the buoyant fluid, and thus can account for an offshore mass transport whether or not the average position of the outcropping shifts. We note that $2(\overline{R} - r_I)$ is a measure of the (non-dimensional) width of the current, taking its thickness into account.

In figure 7(*a*) we plot $\overline{R}^*(t^*)$, the dimensional version of $\overline{R}(t)$, for the five simulations in SERIES 1. Lateral growth of the jet is similar for simulations step1-I and flat1, suggesting that step topography plays a minor role if it is located shoreward of the outcropping. Simulations slope1-I and slope1-O demonstrate a somewhat more

vigorous instability and faster spreading of buoyant fluid. This is at variance with CL's experiments, which showed a suppression of instability in the presence of a slope. However, our theory neglects some aspects of the instability process, most notably Ekman and Stewartson layers and a mean flow in the ambient fluid. Boundary layers would not be easy to incorporate in the model, and specification of an ambient mean flow would involve some arbitrary choices, which we wished to avoid. The most dramatic response to topography in our simulations is seen for simulation step1-O (dotted line in figure 7*a*), in which radial spreading as measured by $\overline{R}^*$ is significantly delayed.

Similar trends with respect to topography are visible in figure 7(*b*), a plot of the volume-integrated upper-layer perturbation kinetic energy,

$$\widetilde{E}_K(t) = \frac{1}{V}\int\!\!\int_{\Omega} h\nabla h' \cdot \nabla h' r \,\mathrm{d}r \,\mathrm{d}\theta, \tag{3.5}$$

where $h(r,\theta,t) = h_0(r) + h'(r,\theta,t)$, using notation introduced in (2.10). Since the frontal profile and lower-layer perturbation were the same in all simulations, we may compare the kinetic energies quantitatively. Simulation flat1 exhibits lower levels of $\widetilde{E}_K$ than step1-I, slope1-I and slope1-O. Simulation step1-O is associated with a drastic reduction in kinetic energy for the majority of the simulation, compared to the other simulations. Again, this trend is consistent with the trend in $\overline{R}^*$, as discussed above. Because the instability in simulation flat1 is free from the complex influence of topographic variations, the corresponding $\widetilde{E}_K$ curve in figure 7(*b*) clearly shows a quasi-periodic cycle of growth and saturation. CL also observed distinct subsequent instability events in some of their experiments, before the buoyant fluid reached the outer boundary.

The eigenvalue problem associated with the linearized equations in rectangular coordinates was solved in Reszka (2003) using a spectral approach. The theory is discussed elsewhere (manuscript in preparation), the results of which may be applied to the present model configuration as follows. If we identify the annulus domain with a straight, x-periodic channel and the axisymmetric current profile (3.1) with an x-invariant jet of the same exponential form, then we may compare the dominant wavelength of the instability with that predicted by linear theory. The instability is always focused near the sharpest frontal gradients, therefore we take the length of the periodic channel to be the initial circumference of the outside edge of the jet (i.e. the length of the outcropping). With our chosen values for α, γ and b, the outcropping has a dimensional length of 144 cm. Using a flat bottom the spectral technique gives a characteristic wavelength λ^* of approximately 6 cm.

Regarding the simulations, table 1 records the values of λ^*, which were obtained by dividing 144 cm by the number of waves observed in the lower layer at the initial stages of instability (as in figure 3*b*). We found that dipoles developing in the lower layer were significantly easier to identify than deformations of the outcropping. The observed wavelength for flat1 is 7.2 cm, which is not far from the linear prediction. Some error is to be expected, given the different geometries employed in the theory and simulations. Also, as noted in Reszka (2003), our solution method seems to overestimate wavenumbers somewhat. Since the assumed eigenproblem can only account for linearly sloping (or flat) topography we are only able to predict the wavelength for simulation flat1.

As table 1 indicates, the dominant wavelength in our simulations was 4–8 times the Rossby radius. Here, we use $R_1 = 0.93$ cm for all simulations, even though in

practice R_1 increased with time in SERIES 2 simulations, due to deepening of the upper layer. On the other hand, CL found that the wavelength of the instability was, on average, 13 times the upper-layer Rossby radius. If we include only the first instability event from each experiment in CL (which is most relevant to our chosen configuration), their data suggest $\lambda^* \approx 10\,\text{cm}$. One should keep in mind that the dominant lengthscale was determined by CL at finite amplitude, i.e. after some merging of the developing anomalies had taken place. Merging also occurs in our simulations, as is evident in figure 2(*a–d*). However, we chose to report the results at the onset of instability, when the number of lower-layer pressure anomalies is the most unambiguous. The wavelengths recorded in table 1 therefore can be expected to underestimate the finite-amplitude lengthscales of CL somewhat.

CL observed that buoyant fluid reached the outer tank wall faster with ridge topography (on the interior side of the front) than with a flat bottom. However, we did not find the rate of spreading to differ significantly in these two cases. We attribute this discrepancy to flow features not accounted for in our theory, such as friction or a non-negligible ambient mean flow (see § 3.1). We also feel that the presence of a source could modify the observed instability characteristics to some degree. CL argue that lateral spreading does not affect the instability due to a timescale separation between the two processes. In the theory of Griffiths & Linden (1981), the growing current is stable until a critical value of the Froude number is reached. It seems that if the current is stable for a period of time, after which it is unstable, then it would have passed through a regime where growth rates are non-zero but small. In such a regime, the timescale of the instability would be similar to that of the spreading, thus allowing the two processes to interact. However, the results of CL are in good agreement with previous laboratory and numerical studies (e.g. Griffiths & Linden 1981, 1982; Verzicco *et al.* 1997) so the effect is at most quantitative.

3.4. *Source flow simulations*

In SERIES 2, the initial condition for the upper layer was the same as in SERIES 1; however the introduction of a source term caused the current to deepen over time, so that its thickness increased to 5.25 cm over 30 rotation periods. The source term $Q(r, \theta)$ was proportional to the initial isopycnal profile (3.1), with its amplitude adjusted to give a total flux $10\,\text{cm}^3\,\text{s}^{-1}$. The resulting compression of vortex tubes in the lower layer induced an anticyclonic azimuthal current in the ambient fluid. In this regard, SERIES 2 simulations are more in keeping with the configuration of CL's experiments. As table 1 shows, the azimuthal wavenumber of the instability was modified in only three simulations, and only by a small amount. Diagnostic quantities, plotted in figures 7(*c*) and 7(*d*), evolved similarly to those in SERIES 1. As exemplified by the weighted jet width $\overline{R}$, spreading of the current was enhanced for sloping topography (also the step topography, step2-I), but was impeded for a ridge located at the outcropping (step2-O). The upper-layer perturbation kinetic energy clearly reflects a delay in lateral penetration in the early stages of instability, as was the case in SERIES 1.

On the other hand, some qualitative differences in behaviour did arise in SERIES 2. These were most pronounced in the flat bottom simulation, flat2, and we plot two pairs of streamfunction snapshots for this case in figure 8. Initially the upper-layer thickness looked the same as in figure 2(*a*), while the lower-layer pressure field was zero everywhere. A growing, wave-like deformation of the outcropping was observed as in SERIES 1; however the associated pressure anomalies in the lower layer did not have a cyclonic component. Gradually, additional horizontal shear developed in

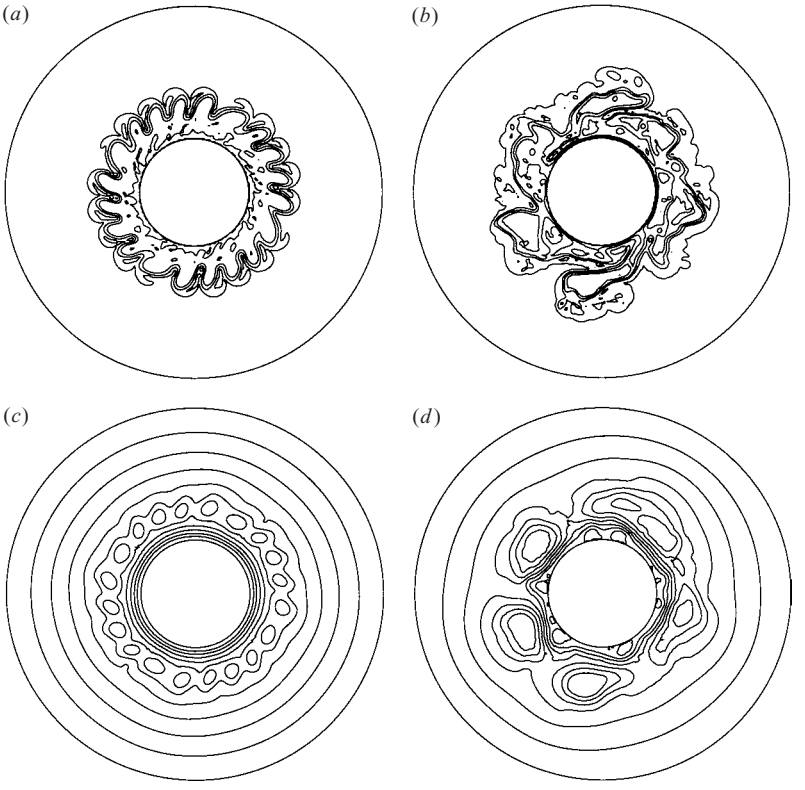

FIGURE 8. Dimensional upper-layer thickness at (*a*) 15 and (*b*) 24 rotation periods; non-dimensional lower-layer pressure at (*c*) 15 and (*d*) 24 rotation periods in simulation flat2. The contour extrema and intervals are, respectively, (*a*) 0, 4.2 and 1.4 cm, (*b*) 0, 4.8 and 1.2 cm, (*c*) 0, 3.6 and 0.6, (*d*) 0, 7.2 and 1.2. The initial profile for the upper layer is exactly as shown in figure 2(*a*).

the radial direction due to the imposed flux. In fact, velocities at the outer edge of the current were high enough to cause the growing meanders to break forward and merge together. In figure 8(*a*) waves that break backward are visible at the extreme edge of the current; however the main body of each emerging anticyclonic eddy leans forward.

The corresponding lower-layer streamfunction (figure 8*c*) exhibits high-pressure cells exclusively. Figure 8 should be compared with figures 2 and 3. No eddies pinch off in this simulation after the waves break, in agreement with observations of CL. Increased anticyclonic vorticity results in continued merging of adjacent features, as well as a more turbulent flow than in SERIES 1. This is evident in figures 8(*b*) and 8(*d*). At late times, the upper layer is dominated by a few large, irregular blobs, which circulate around the inner wall. Some of these detach by the end of the simulation, at $t/P = 30$.

3.5. *Eddy transports*

The instability we have described leads to a general outward spreading of the buoyant fluid, as discussed in § 3.3. However, we have not found a preferred direction of azimuthal motion for isolated eddies in either series of simulations. Frequent collisions between the vortices and interactions with the jet typically obscure any

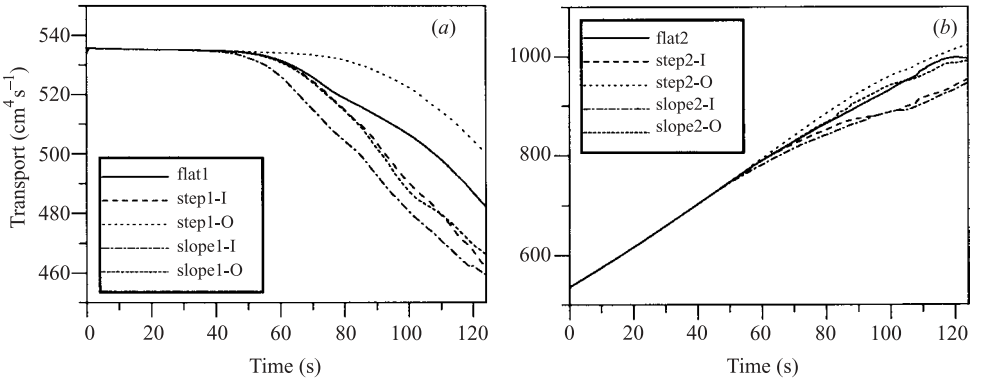

FIGURE 9. Total dimensional upper-layer azimuthal flux for (*a*) SERIES 1 and (*b*) SERIES 2.

overall drift. Eddies that manage to remain isolated usually maintain a stationary position with respect to the rotating coordinate frame, or are advected in curved paths by cyclonic recirculations between meander crests. In the oceanographic context, this raises the possibility that, in the long term, detached lenses may affect the total along-coast mass flux.

We define the total non-dimensional upper-layer azimuthal transport $T_\theta(t)$ as

$$T_\theta(t) = -\int\!\!\int_\Omega rhu_{1\theta}\,\mathrm{d}r\,\mathrm{d}\theta, \tag{3.6}$$

where the minus sign in front of the integral simply ensures that the transport will be positive for frontal profiles with $\mathrm{d}h_0/\mathrm{d}r < 0$. In figure 9 we plot $T^*_\theta(t^*)$, the dimensional counterpart of (3.6). For SERIES 1, the magnitude of the average transport diminishes over time by as much as 16% (figure 9*a*). Thus the eddies have a small, but non-negligible, effect on T^*_θ. We note that the transport diminishes least for simulation step1-O, which is consistent with the delay in destabilization (and subsequent eddy formation) discussed above.

In SERIES 2, the source flux induces an increasingly strong clockwise flow, which dominates over eddy fluxes. In this case the total transport increases for all simulations by a factor of approximately 2, over the course of the simulation (figure 9*b*). As noted before, simulations involving a source are relevant to the experiments of CL and Griffiths & Linden (1981). Anticyclonic vorticity induced by the injection, as well as the increase in the effective deformation radius due to deepening of the buoyant layer, seem to inhibit eddy pinch-off, corroborating CL's findings. The effect is even more pronounced than it would be in the laboratory setting since, in the present model, there is no lateral spreading associated with the source. (As explained in § 3.1, the velocity simply follows streamlines). Actual coastal currents whose depth remains quasi-steady are likely to spawn vortices more readily than SERIES 2 suggests. However, judging from figure 9(*a*), the associated along-shore transport is unlikely to be affected by eddy shedding to a significant degree.

4. Discussion

The QG formalism makes several simplifying assumptions, such as those of small interfacial displacements and topographic gradients, which are often too restrictive to be applied in actual laboratory or oceanographic settings associated with coastally

trapped currents. Nevertheless, it does offer a useful theoretical framework for understanding many of the physical processes involved in baroclinic dynamics. Indeed, Griffiths & Linden (1981) used a modified version of the Phillips model (Pedlosky 1987) to explain the instability they observed, and CL reported general agreement between their results and those of the Griffiths & Linden (1981) theory.

Let us consider the traditional inviscid two-layer QG channel model that includes topography and the β-plane, where y is the cross-channel coordinate. The cross-channel PV gradients in the upper and lower layer are, respectively,

$$\frac{\partial q_1}{\partial y} = F_1(u_1 - u_2) - u_{1yy} + \beta, \tag{4.1a}$$

$$\frac{\partial q_2}{\partial y} = F_2(u_2 - u_1) - u_{2yy} + \beta + h_{By}, \tag{4.1b}$$

where, for $i = 1, 2$, q_i, F_i, u_i are the potential vorticities, Froude numbers and along-channel velocities, respectively. Here β is the usual β parameter and $h_B(y)$ is a scaled topography term. If the flow in the upper layer is y-independent and is zero in the lower layer, then we may write

$$\frac{\partial q_1}{\partial y} = F_1 u_1 + \beta, \tag{4.2a}$$

$$\frac{\partial q_2}{\partial y} = -F_2 u_1 + \beta + h_{By}. \tag{4.2b}$$

The necessary condition for instability is that the PV gradient be somewhere positive and somewhere negative (Pedlosky 1964). It is not necessary that either PV gradient vanish somewhere, only that the gradients be of opposite sign.

It is well-known that increasing β stabilizes the system to infinitesimal perturbations (Orlanski 1969). It is easy to see from (4.2*a*), (4.2*b*) that as β increases, eventually both gradients become positive everywhere, thus meeting the sufficient criterion for stability. The influence of the topographic term, however, is not unambiguous, since this term occurs only in q_2, and its gradient may be positive or negative. Here, let us make the f-plane approximation $\beta = 0$, and assume that $u_1 > 0$. The latter condition corresponds to an interface that rises in the offshore direction and a positive q_{1y}. In this case, sufficiently large h_{By} will force $q_{2y} > 0$, thus stabilizing the fluid. Conversely, for h_{By} small enough, q_{2y} becomes negative, thus meeting the necessary condition for instability. These conditions are exactly analogous to the ones derived in § 2.2.

Experience shows that the above system is unstable in some parameter regimes where the instability condition is met. Assuming that the dependence of the instability characteristics on the topographic gradient is continuous, one may suppose, for $u_1 > 0$, that growth rates will increase with decreasing h_{By}. Indeed, this is the general trend we observe in our simulations, comparing the flat and sloping topography cases (see also Reszka & Swaters 1999). If we identify a sector of the annulus with a channel, where x and y are the along-shore and off-shore directions, then the configuration of the basic flow in our simulations satisfies $u_1 > 0$, $h_{By} \leqslant 0$. (We point out that, for such a mapping, the right-hand side in definition (2.9) for the along-shore velocity requires multiplication by a minus sign because of the traditional direction of positive θ in the (r, θ) coordinate system). In this sense, the flows described in our numerical simulations satisfy both the QG necessary condition for instability, above, as well as condition (2.22).

However, as CL point out, a necessary condition for instability does not ensure instability, and other criteria may come into effect depending on the details of

the flow. Additional criteria were found in the two-layer shallow-water context by Barth (1989), although his study only considered upwelling fronts. The investigations of Flagg & Beardsley (1978), Mechoso & Sinton (1981) and Gawarkiewicz (1991) clearly demonstrate that factors such as mean flows, large-amplitude topography, and the shape of the topography all compete in determining the growth rate. Three basic topographic profiles were considered here, although many others are possible. The influence of a mean flow could be investigated in an extension of the present study.

Almost certainly, flow evolution in a laboratory environment will be much more complex than the simple arguments above suggest. Our discussion with respect to QG dynamics and the governing equations (2.5*a*), (2.5*b*) has neglected the existence of lateral shear in the mean flow, friction at the bottom boundary and sidewalls, as well as Ekman draining. As we pointed out in § 3, a constant source of buoyant fluid and a non-negligible outward pressure gradient may also affect the instability. Recently, Sutherland *et al.* (2003) performed detailed laboratory experiments in order to investigate the related problem of instability in bottom-trapped baroclinic currents. They found that growth of the baroclinic layer through gradual injection of fluid induced significant motion in the ambient layer, and the resulting dynamics turned out to be largely barotropic. If a similar process occurred in the experiments of CL, then our assumption of a quiescent ambient is not entirely appropriate, which may explain why we find (unlike CL) that sloping topography is generally a destabilizing, rather than a stabilizing, influence.

On the other hand, our simulations corroborate the observation of CL that step topography inhibits vortex growth and pinch-off, at least when the step is located on the offshore side of the front. The buoyant fluid is then trapped, temporarily, on the shoreward side of the ridge. A likely reason for this behaviour is that motion across the ridge (or any steep topography) would require significant changes in the relative vorticity of the fluid, due to conservation of PV (CL). Such drastic increases/decreases in relative vorticity were not observed by CL, and they concluded that lower-layer fluid must be draining radially outward through an Ekman-like layer along the topography. This mechanism is clearly absent in our model. In our simulations motion across the ridge was delayed until the front had released enough potential energy. In a real oceanographic setting, tidal and wind forcings are likely to interrupt the instability, therefore this mechanism may be partly responsible for the persistence of shelf-break fronts.

Each of our numerical experiments lasted no more than about 30 rotational periods. This is considerably less than the total duration of the laboratory experiments of CL. The reasons for this are as follows. As explained previously, our simulations start with a fully formed, geostrophically adjusted buoyant current. Also, CL followed the evolution of the current through secondary instabilities and up to the time when the buoyant fluid reached the outer boundary. In order to fully describe these long-term processes, a model with more complete dynamics should be utilized. We feel that the relatively simple model used here is applicable to the initial instability and eddy generation process, but its relevance to later stages of flow development would be tentative, mainly due to the lack of down-pressure-gradient forces in the governing equations.

Griffiths & Linden (1981) and CL determined that the dominant wavelength of the instability in their experiments was inversely proportional to the rotational Froude number associated with the buoyant fluid. The frontal geostrophic approximation used here was derived implicitly assuming a large Froude number and therefore this parameter does not appear in the leading-order balance (2.5*a*), (2.5*b*). However, a relationship between lengthscales and the Froude number can be obtained using a simple scaling argument. Treating f_0, L, g' and H as external parameters that do not

depend on δ, definition (1.1) implies that $F = (f_0 L)^2/(\delta g' H) \sim \delta^{-1}$. Our assumption of small δ implies that the present model is applicable in the large Froude number regime. Furthermore, we obtain from (2.1) that $L_* = \delta^{1/4} R_2 \sim \delta^{1/4}$ where again R_2 is independent of δ. Thus, heuristically, we would expect $L_* \sim F^{-1/4}$ in the present theory, i.e. an inverse relationship between the model lengthscale and Froude number. We have not tested this argument numerically; however it may be of interest to do so in the future.

5. Conclusions

We have presented numerical simulations of initially axisymmetric buoyant currents in the presence of topography, using a two-layer frontal geostrophic model. The three kinds of idealized topography considered were flat, shelf-ridge and shelf-slope. The current associated with the sloping front became unstable for all topographic configurations, where the instability was manifested as backward-breaking waves in the frontal layer and dipole eddies in the ambient fluid. This behaviour is consistent with observations described in Griffiths & Linden (1981) and CL. For simulations without a source of buoyant fluid the meandering current generated coherent eddies, which moved radially outward. Eddy pinch-off was inhibited in source-flow simulations, in agreement with CL.

It was found that topography which generally slopes in the opposite sense to the front has a destabilizing effect. While this result is consistent with a necessary condition for instability for this model (as well as the analogous QG criterion), CL found that sloping topography inhibited instability. The discrepancy may be due to one of several factors, such as the neglect in our theory of frictional boundary layers or the assumption of a deep, initially quiescent ambient layer. Nevertheless, we found that step topography traps buoyant fluid and inhibits radial motions, in agreement with the findings of CL. The present theory can only account for the baroclinic aspects of the initial instability. However, since both CL and Griffiths & Linden (1981) believed the instability to be primarily baroclinic, we feel that the flow evolution we have described is pertinent in these cases.

Laboratory experiments invariably involve some motion in the ambient fluid before the onset of instability, especially in cases involving constant injection of buoyant fluid (Griffiths & Linden 1981; Sutherland *et al.* 2003). Here, we wanted to examine the simplest scenario, in which the lower layer is initially motionless and the dynamics predominantly baroclinic. In the future, however, we would like to investigate the effect of mean flows in the ambient fluid, and the possibility of mixed barotropic–baroclinic instability.

The authors wish to thank Paul Choboter for many helpful discussions regarding various aspects of this research. This work was supported in part by a research grant awarded to G.E.S. by the Natural Sciences and Engineering Research Council of Canada (NSERC), as well as a PhD Dissertation Scholarship and an Andrew Stewart Memorial Graduate Prize awarded to M.K.R. by the University of Alberta.

REFERENCES

Arakawa, A. 1966 Computational design for long term numerical integration of the equations of fluid motion: Two-dimensional incompressible flow. *J. Comput. Phys.* **1**, 119–143.

Barth, J. A. 1989 Stability of a coastal upwelling Front. 2. Model results and comparison with observations. *J. Geophys. Res.* **94**, 10857–10883 .

Cenedese, C. & Linden, P. F. 2002 Stability of a buoyancy-driven coastal current at the shelf break. *J. Fluid Mech.* **452**, 97–121 (referred to herein as CL).

Church, J. A., Cresswell, G. R. & Godfrey, J. S. 1989 The Leeuwin Current. In *Poleward Flows Along Eastern Ocean Boundaries* (ed. S. J. Neshyba *et al.*). Coastal and Estuarine Studies, vol. 34, pp. 230–252. Springer.

Cushman-Roisin, B. 1986 Frontal Geostrophic Dynamics. *J. Phys. Oceanogr.* **22**, 117–127.

Cushman-Roisin, B., Sutyrin, G. G. & Tang, B. 1992 Two-layer geostrophic dynamics. Part I: Governing equations. *J. Phys. Oceanogr.* **20**, 758–768.

Flagg, C. N. & Beardsley, R. C. 1978 On the stability of the shelf water/slope water front south of New England. *J. Geophys. Res.* **83**, 4623–4631.

Gawarkiewicz, G. 1991 Linear stability models of shelfbreak fronts. *J. Phys. Oceanogr.* **21**, 471–488.

Griffiths, R. W. & Linden, P. F. 1981 The stability of buoyancy-driven coastal currents. *Dyn. Atmos. Oceans* **5**, 281–306.

Griffiths, R. W. & Linden, P. F. 1982 Laboratory experiments on fronts. Part I. Density-driven boundary currents. *Geophys. Astrophys. Fluid Dyn.* **19**, 159–187.

Hallberg, R. & Gnanadesikan, A. 2001 An exploration of the role of transient eddies in determining the transport of a zonally reentrant current. *J. Phys. Oceanogr.* **31**, 3312–3330.

Johannessen, J. A., Svendsen, E., Sandven, S., Johannessen, O. M. & Lygre, K. 1989 Three-dimensional structure of mesoscale eddies in the Norwegian coastal current. *J. Phys. Oceanogr.* **19**, 3–19.

Karsten, R. H. & Swaters, G. E. 1999 A unified asymptotic derivation of two-layer frontal geostrophic models including planetary sphericity and variable topography. *Phys. Fluids* **11**, 2583–2597.

Karsten, R. H. & Swaters, G. E. 2000 Nonlinear effects in two-layer large-amplitude geostrophic dynamics. Part 1. The strong-beta case. *J. Fluid Mech.* **412**, 125–160.

Kincaid, D. & Cheney, W. 1996 *Numerical Analysis.* Brooks/Cole.

Masson, D. & Cummins, P. F. 1999 Numerical simulations of a buoyancy-driven coastal countercurrent off Vancouver Island. *J. Phys. Oceanogr.* **29**, 418–435.

Mechoso, C. R. & Sinton, D. M. 1981 Instability of baroclinic flows with horizontal shear along topography. *J. Phys. Oceanogr.* **11**, 813–821.

Mertz, G., Gratton, Y. & Gagné, J. A. 1990 Properties of unstable waves in the St. Lawrence Estuary. *Atmos.-Ocean* **28**, 230–240.

Orlanski, I. 1969 The influence of bottom topography on the stability of jets in a baroclinic fluid *J. Atmos. Sci.* **26**, 1216–1232.

Paldor, N. & Ghil, M. 1991 Shortwave instabilities of coastal currents. *Geophys. Astrophys. Res.* **58**, 225–241.

Pedlosky, J. 1964 The stability of currents in the atmosphere and the ocean: Part I. *J. Atmos. Sci.* **21**, 201–219.

Pedlosky, J. 1987 *Geophysical Fluid Dynamics.* Springer.

Pingree, R. D. & LeCann, B. 2000 Three anticyclonic slope water oceanic eDDIES (SWODDIES) in the Southern Bay of Biscay in 1990. *Deep-Sea Res.* **39**, 1147–1175.

Reszka, M. K. 2003 Baroclinic frontal dynamics in the presence of stratification and topography. PhD thesis. University of Alberta.

Reszka, M. K. & Swaters, G. E. 1999 Numerical investigation of baroclinic instability in the Gaspé current using a frontal geostrophic model. *J. Geophys. Res.* **104**, 25685–25696.

Sutherland, B. R., Nault, J., Yewchuk, K. & Swaters, G. E. 2003 Rotating dense currents on a slope. Part 1. Stability. *J. Fluid Mech.* (submitted).

Swaters, G. E. 1993 On the baroclinic dynamics, Hamiltonian formulation and general stability characteristics of density-driven currents and fronts over a sloping continental shelf. *Phil. Trans. R. Soc. Lond.* A **345**, 295–325.

Tang, B. & Cushman-Roisin, B. 1992 Two-layer geostrophic dynamics. Part II: Geostrophic Turbulence. *J. Phys. Oceanogr.* **22**, 128–138.

Verzicco, R., Lalli, F. & Campana, E. 1997 Dynamics of baroclinic vortices in a rotating, stratified fluid: A numerical study. *Phys. Fluids* **9**, 419–432.

Wadhams, P., Gill, A. E. & Linden, P. F. 1979 Transects by submarine of the East Greenland Polar Front. *Deep-Sea Res.* **26**, 1311–1327.